Nanoscale

Accepted Manuscript

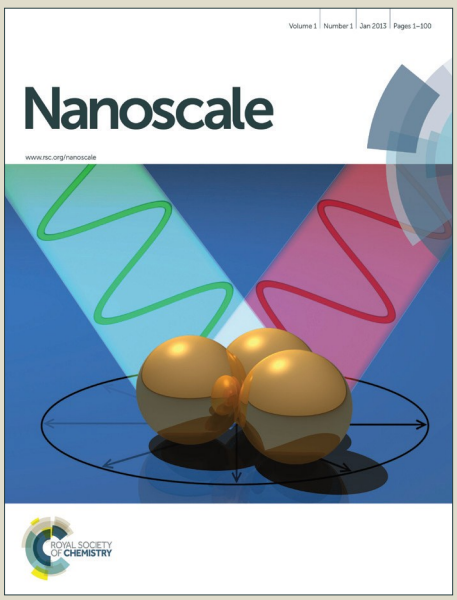

ROYAL SOCIETY OF CHEMISTRY

www.rsc.org/nanoscale

Optimum designs of a nanoscale spin Seebeck power device

Tianjun Liao[1], Jian Lin[1], Guozhen Su[1], Bihong Lin[2], Jincan Chen[1,*]

[1]Department of Physics, Xiamen University, Xiamen 361005, People's Republic of China

[2]College of Information Science and Engineering, Huaqiao University, Xiamen 361021, People's Republic of China

Abstract: A theoretical model of the nanoscale spin-Seebeck power device (SSPD) is proposed based on the longitudinal spin-Seebeck effect in bilayers made of a ferromagnetic insulator and a normal metal. Expressions for the power output and thermal efficiency of the SSPD are derived analytically. The performance characteristics of the nanoscale SSPD are analyzed by using the numerical simulation. The maximum power output density and efficiency are calculated numerically. The effect of the spin Hall angle on performance characteristics of the SSPD is analyzed. The choice of materials and the structure of the device are discussed. The optimum criteria of some key parameters of the SSPD, such as the power output density, efficiency, thickness of the normal metal, and load resistance, are given. The results obtained here can provide a theoretical basis for the optimal design and operation of nanoscale SSPDs.

Key words: Spin-Seebeck effect; Spintronics; Spin caloritronics; Inverse spin Hall effect; Nanoscale

* jcchen@xmu.edu.cn

1. Introduction

The conventional semiconductor thermoelectric generator is able to convert a part of the heat absorbed by the hot junction of the thermoelectric device directly into electrical power, based on the Seebeek effect [1]. Recently, the spin-Seebeck effect (SSE) involving spintronics and spin calorironics was proposed by Uchida who observed the spin current induced by the temperature gradient in the metallic magnet and the spin voltage generated by the inverse spin Hall effect in the normal metal [2]. The analogous SSEs were investigated theoretically and experimentally in the ferromagnetic metal [3], ferromagnetic zigzag α -graphyne nanoribbons [4], ferromagnetic semiconductor [5], ferromagnet superconductor junction [6], and ferromagnetic insulator [7]. The mechanism of the SSE is that a temperature difference between the magnons in the magnetic insulator and the electrons in the metal contact leads to thermal pumping of a spin current. This spin current is transformed into an observable voltage by the inverse spin Hall effect [8]. On the other hand, the theories of spin-pumping [9], phonon-drag spin current [10], magnon-drag spin current [11], and acoustic spin pumping [12] were applied to investigate the SSE and design the spin nano-devices such as the nanoscale spin Seebeck effect diode [13], spin thermoelectric coating [14], spin valve [15], magnetic tunneling junction [16], spin wave logic device [17], spin field effect transistor [18], etc. The spin current produced by the SSE can be perpendicular or parallel to the temperature gradient, so the SSE can be divided into two types: transverse and longitudinal SSEs [19]. The longitudinal SSE was observed in the structure with a ferromagnetic insulator material in contact with a normal metal and investigated intensively by many researchers in the recent years [19-28]. Uchida *et al.* observed firstly the longitudinal SSE in the device composed of an $Y_3Fe_5O_{12}$ (YIG) and a Pt film and discovered a spin current generated in the Pt film along the temperature gradient and a spin voltage generated at the YIG/Pt interface [20]. They studied the longitudinal SSE in various garnet ferrite samples $Y_{3-x}R_xFe_{5-y}M_yO_{12}$ (R=Gd, Ca; M=Al, Mn, V, In, Zr). The obtained results showed that the longitudinal SSE voltage in those samples has a positive correlation with the Curie temperature and the saturation magnetization,

but no clear correlation with the gyromagnetic ratio and the Gilbert damping constant of the samples [21]. Agrawal *et al.* experimentally verified the magnon spin-current theory for the longitudinal SSE in the YIG/Pt system [22]. Kikkawa *et al.* proved that intrinsic longitudinal SSE in Au/YIG and Pt/Cu/YIG systems are free from the anomalous Nernst effect caused by an extrinsic proximity effect and showed that the longitudinal SSE appears even when the mechanism of the proximity Nernst effect is clearly removed [23]. Xu *et al.* designed devices NiFe/Cu/Pd(Ta) that can convert the heat-driven spin current to a transverse electric voltage and isolated the longitudinal SSE, anomalous Nernst effect generated by the ferromagnetic metal, and anomalous Nernst effect induced by proximity in the non-magnetic metal [24]. Mendes *et al.* investigated experimentally the longitudinal SSE in YIG/$Ir_{20}Mn_{80}$ and compared it with YIG/Pt. The obtained results showed that $Ir_{20}Mn_{80}$ has a spin Hall angle similar to Pt, the voltage generated in $Ir_{20}Mn_{80}$ by the inverse spin Hall effect is quite larger than that in Pt [25]. Rezende *et al.* proposed a model for controlling the heat of the spin pumping damping and calculating the distributions of the temperatures of the magnon, phonon, and electron in ferromagnetic insulator/normal metal hybrid structures [26, 27]. Li *et al.* presented a significant structure composed of a hexagonal ferrite thin film $BaFe_{12}O_{19}$, a Pt, and a sapphire substrate, which can be applied to the spin battery that converts light into electric voltage [28]. Recently, Flipse observed the spin Peltier effect in magnetic insulators and verified the reciprocity between the SSE and the spin Peltier effect [29]. The discovery of the spin Peltier effect is attractive for designing nanoscale thermoelectric generators and refrigerators. In addition, Cahaya [30] proposed two models of the spin Seebeck power device (SSPD) and derived expressions for the efficiency of the SSPD based on spintronics and spin caloritronics. By using the thermal analysis method of the conventional thermoelectric generator, the figures of merit of two SSPDs were estimated.

In the present paper, the performance characteristics of a nanoscale SSPD are investigated. The maximum power output density and efficiency are calculated. The optimum problems related to the choice of materials, geometry structure of the normal metal, and matching of the load resistance are discussed in detail. The choice

criteria of key parameters are given.

2. Model description

The model and effective circuit of the SSPD consisting of a ferromagnetic insulator, a normal metal, a load resistance R_L, and an external magnetic field H are shown in Fig. 1, where M is the magnetization, R_I and E are the internal resistance and electromotive force of the SSPD, J_S and J_Q are the spin current and average heat flow, J_c and V are the average transverse charge current and transverse voltage across R_L, d_F and d_N are the thicknesses of the ferromagnetic insulator and normal metal, L and W are the length and width of the ferromagnetic insulator/normal metal bilayer. Fig. 1(a) shows clearly that when the external magnetic field is applied to the x direction, a temperature gradient between the ferromagnetic insulator and the normal metal leads to a part of the heat flow J_Q to convert into a spin current J_S [29], which can be transformed into the charge current J_c in the normal metal with the help of the inverse spin Hall effect, and the average transverse charge current J_c goes through an external resistance to generate electricity power. It should be pointed out that the amount of the spin current flowing through the ferromagnetic insulator/normal metal interface is governed by the complex spin-mixing conductance $G_{\uparrow\downarrow}$. It is assumed in the model that H is parallel to M (the angle between the magnetic field and the magnetization $\alpha = 0^0$).

3. Power output and efficiency

The magnon temperature $T_{\mathrm{m}}(z)$ and phonon temperature $T_{\mathrm{p}}(z)$ obey the following equations [27, 31-35]

$$\frac{d^2 T_{\mathrm{m}}(z)}{dz^2} + \frac{c_{\mathrm{p}} c_{\mathrm{m}}}{c_{\mathrm{T}}} \frac{1}{\kappa_{\mathrm{m}} \tau_{\mathrm{mp}}} \left[T_{\mathrm{p}}(z) - T_{\mathrm{m}}(z) \right] = 0 \tag{1}$$

and

$$\frac{d^2 T_{\mathrm{p}}(z)}{dz^2} + \frac{c_{\mathrm{p}} c_{\mathrm{m}}}{c_{\mathrm{T}}} \frac{1}{\kappa_{\mathrm{p}} \tau_{\mathrm{mp}}} \left[T_{\mathrm{m}}(z) - T_{\mathrm{p}}(z) \right] = 0, \tag{2}$$

where c_{m}, c_{p}, and $c_{\mathrm{T}} = c_{\mathrm{m}} + c_{\mathrm{p}}$ are the magnon, phonon, and total heat capacities per unit volume, κ_{m} and κ_{p} are the magnon and phonon thermal conductivities, and τ_{mp} is the magnon-phonon relaxation time. Because there are a substrate attached to the bottom ($z = -d_{\mathrm{F}}$) of the ferromagnetic insulator and normal metal on the top ($z = 0$) of the ferromagnetic insulator, it may be assumed that fixed phonon temperatures $T_{\mathrm{b}}^{\mathrm{p}} = \mathrm{const}$ at $z = -d_{\mathrm{F}}$ and $T_{\mathrm{t}}^{\mathrm{p}} = \mathrm{const}$ at $z = 0$, and that the phonon temperature is equal to the electron temperature at two interfaces, i.e., $T_{\mathrm{b/t}} = T_{\mathrm{b/t}}^{\mathrm{p}} = T_{\mathrm{b/t}}^{\mathrm{e}} = \mathrm{const}$, where subscripts b/t indicate bottom and top. The boundary conditions of the phonon and magnon systems are, respectively, given by [35]

$$\begin{cases} -\kappa_{\mathrm{p}} \left. \dfrac{dT_{\mathrm{p}}(z)}{dz} \right|_{z=-d_{\mathrm{F}}} = \kappa_{\mathrm{th,b}}^{\mathrm{p}} \left[T_{\mathrm{b}} - T_{\mathrm{p}}\left(-d_{\mathrm{F}}\right) \right] \\ -\kappa_{\mathrm{p}} \left. \dfrac{dT_{\mathrm{p}}(z)}{dz} \right|_{z=0} = \kappa_{\mathrm{th,t}}^{\mathrm{p}} \left[T_{\mathrm{p}}(0) - T_{\mathrm{t}} \right] \end{cases} \tag{3}$$

and

$$\begin{cases} -\kappa_{\mathrm{m}} \left. \dfrac{dT_{\mathrm{m}}(z)}{dz} \right|_{z=-d_{\mathrm{F}}} = \kappa_{\mathrm{th,b}}^{\mathrm{m}} \left[T_{\mathrm{b}} - T_{\mathrm{m}}\left(-d_{\mathrm{F}}\right) \right] \\ -\kappa_{\mathrm{m}} \left. \dfrac{dT_{\mathrm{m}}(z)}{dz} \right|_{z=0} = \kappa_{\mathrm{th,t}}^{\mathrm{m}} \left[T_{\mathrm{m}}(0) - T_{\mathrm{t}} \right] \end{cases}, \tag{4}$$

where $\kappa_{\mathrm{th,b}}^{\mathrm{p}}$ and $\kappa_{\mathrm{th,t}}^{\mathrm{p}}$ are the phonon interfacial thermal conductances, and $\kappa_{\mathrm{th,b}}^{\mathrm{m}}$ and $\kappa_{\mathrm{th,t}}^{\mathrm{m}}$ are the magnon interfacial thermal conductances. With the help of these boundary conditions, $T_{\mathrm{m}}(0)$ can be calculated from Eqs. (1) and (2).

Based on the above theory, the SSE current J_S pumped from the ferromagnetic insulator into the normal metal is proportional to the temperature difference $\Delta T = T_{\mathrm{t}}^{\mathrm{e}} - T_{\mathrm{m}}(0)$ and the interface spin Seeebeck coefficient L_S and is given by [29, 30]

$$J_S = L_S \left[T_{\mathrm{m}}(0) - T_{\mathrm{t}}^{\mathrm{e}} \right], \tag{5}$$

where $L_S = \hbar k_B G_r \gamma / \left(e M_s V_c 2\pi \right)$, $\hbar$ is the reduced Planck constant, e is the elementary positive charge, γ is the gyromagnetic ration, M_s is the saturation magnetization, k_B is the Boltzmann constant, G_r is the real

part of the spin mixing conductance $G_{\uparrow\downarrow}$ [36], and V_c is the magnetic coherence volume [35].

Because the Onsager symmetry can be reflected by a linear response matrix, the spin current and average heat flow over the ferromagnetic insulator/normal metal interface are given by [30]

$$\begin{pmatrix} J_s \\ J_Q \end{pmatrix} = \begin{pmatrix} G_S & L_S T \\ L_S T & \left(K + L_S \prod_S\right) T \end{pmatrix} \begin{pmatrix} -\mu_S/2e \\ -\Delta T/T \end{pmatrix}, \tag{6}$$

where $\mu_s = \mu_\uparrow - \mu_\downarrow$ is the spin accumulation, $\mu_\uparrow$ and $\mu_\downarrow$ are spin-up and spin-down electrochemical potentials, $\prod_S = S_S T$ is the spin Peltier coefficient due to the Onsager reciprocity, $T = \left[T_{\mathrm{m}}(0) + T_{\mathrm{t}}^{\mathrm{e}}\right]/2$, $S_S = L_S/G_S$ is the spin Seebeck coefficient, G_S is the interface spin injection conductance, and K is the thermal conductance coefficient in the ferromagnetic insulator/normal metal interface.

The relation between the transverse charge current density $\vec{j}_c(z) = \vec{J}_c(z)/(d_N W)$ and the spin current density $\vec{j}_s(z) = \vec{J}_s(z)/A$ inside the normal metal at distance z induced by the inverse spin Hall effect can be given by [11]

$$\vec{j}_c(z) = \theta_{SH}\vec{j}_s(z) \times \hat{m}, \tag{7}$$

where $A = LW$ is the area of the ferromagnetic insulator/normal metal interface, $\hat{m}$ is the spin-polarization vector, and the spin Hall angle θ_{SH} quantifies the conversion efficiency from the spin to the charge current and is determined by the ratio of the spin Hall conductance to the charge conductance.

The spin current and charge current densities in the normal metal can be given by [30]

$$\begin{pmatrix} j_c \\ j_s \end{pmatrix} = -\sigma_N \begin{pmatrix} 1 & \theta_{SH} \\ -\theta_{SH} & 1 \end{pmatrix} \begin{pmatrix} \partial(\mu_c/e)/\partial y \\ \partial(\mu_s/2e)/\partial z \end{pmatrix}, \tag{8}$$

where $\mu_c = (\mu_\uparrow + \mu_\downarrow)/2$ is the charge electrochemical potential and σ_N is the spin conductivity.

The spin accumulation μ_s obeys the spin diffusion equation in the normal metal [37], i.e.,

$$\nabla^2 \mu_s = \mu_s/\lambda^2, \tag{9}$$

where $\lambda = \sqrt{D\tau_s}$ is the spin-flip relaxation length, τ_s is the spin relaxation time, and D is the spin diffusion coefficient.

By using boundary conditions $j_s(z=0)=J_S/A$ and $j_s(d_N)=0$, the spin diffusion equation can be expressed as [30]

$$\frac{\mu_s}{2e}=\frac{1}{a_1}\left[\theta_{SH}V\frac{\lambda}{L}\left(G_S\sinh\frac{z}{\lambda}+G_N\cosh\frac{z}{\lambda}\right)-\left(\theta_{SH}VG_N\frac{\lambda}{L}+L_S\Delta T\right)\cosh\frac{d_N-z}{\lambda}\right], \tag{10}$$

where $V=-(L/e)\partial\mu_c/\partial y$ is the induced transverse voltage, $G_N=\sigma_N WL/\lambda$ is the spin conductance, and $a_1=G_S\cosh(d_N/\lambda)+G_N\sinh(d_N/\lambda)$

By using Eqs. (8) and (10), the relation between the average transverse charge current J_c and the transverse voltage V in the normal metal is derived as [30]

$$J_c=\frac{1}{d_N}\int_0^{d_N}j_c d_N W dz=-\frac{G_N\lambda}{L}\left(\frac{L_S}{a_2}\theta_{SH}\Delta T\tanh\frac{d_N}{2\lambda}+\frac{d_N V}{L}+a_3\frac{\theta_{SH}^2\lambda V}{L}\right), \tag{11}$$

where $a_2=G_N+G_S\coth\frac{d_N}{\lambda}$ and $a_3=(G_S+2G_N\tanh\frac{d_N}{2\lambda})/(G_N+G_S\coth\frac{d_N}{\lambda})$.

Equation (11) shows that the average transverse charge current J_c is not an independent variable but a function of variables d_N, L, and V. When the circuit is opened, J_c=0 and the open voltage V_{open} is given by

$$V_{open}=\frac{-LL_S\theta_{SH}\Delta T}{a_2\lambda\left(d_N/\lambda+\theta_{SH}^2a_3\right)}\tanh\frac{d_N}{2\lambda}, \tag{12}$$

which varies with d_N/λ and L/λ for other given parameters, while $V_{open}\lambda/L$ is only a function of d_N/λ. It is seen from Eq. (12) that both V_{open} and $V_{open}\lambda/L$ are not of monotonic functions of d_N/λ. When d_N/λ=0 or $d_N/\lambda\to\infty$, both V_{open} and $V_{open}\lambda/L$ are equal to zero. This means that there exists an optimal value of d_N/λ at which both V_{open} and $V_{open}\lambda/L$ attain their maximums, as shown in Fig. 2. When the circuit is shortened, V=0 and the average transverse charge current $J_{c,sh}$ at the short circuit is given by

$$J_{c,sh}=-\frac{\lambda}{L}\frac{L_S}{a_2}\tanh\frac{d_N}{2\lambda}G_N\theta_{SH}\Delta T, \tag{13}$$

which varies with d_N/λ and L/λ for other given parameters, while $J_{c,sh}L/\lambda$ increases with the increase of d_N/λ, as shown in Fig.3, showing both $J_{c,sh}$ and $J_{c,sh}L/\lambda$ are of monotonically increasing functions of d_N/λ.

By using Eq. (11), the power output P of the SSPD is expressed as

$$P=(V_{open}-R_IJ_c)J_c=VJ_c=-\frac{G_NV\lambda}{L}\left[\theta_{SH}\Delta T\frac{L_S}{a_2}\tanh\frac{d_N}{2\lambda}+\frac{V\lambda}{L}\left(\frac{d_N}{\lambda}+a_3\theta_{SH}^2\right)\right], \quad (14)$$

where R_I is the internal resistance of the SSPD and $R_IJ_c^2$ is the Joule heating produced by the electric current flowing through the internal resistance. By substituting $z=0$ into Eq. (10) and combining Eq. (6), the averaged heat in the ferromagnetic insulator/normal metal interface is given by

$$J_Q=-\frac{L_ST}{a_1}\left[\theta_{SH}G_N\frac{V\lambda}{L}\left(1-\cosh\frac{d_N}{\lambda}\right)-L_S\Delta T\cosh\frac{d_N}{\lambda}\right]-\Delta T\left(L_SS_ST+K\right), \quad (15)$$

and consequently, the efficiency of the SSPD can be expressed as

$$\eta=\frac{P}{J_Q}=\frac{c_1\left(V\lambda/L\right)^2+c_2\left(V\lambda/L\right)}{c_3\left(V\lambda/L\right)+c_4}, \quad (16)$$

where $c_1=G_N\left(\frac{d_N}{\lambda}+a_3\theta_{SH}^2\right)$, $c_2=G_N\theta_{SH}\Delta T\frac{L_S}{a_2}\tanh\frac{d_N}{2\lambda}$, $c_3=\frac{L_ST\theta_{SH}G_N}{a_1}\left(1-\cosh\frac{d_N}{\lambda}\right)$, and $c_4=\Delta T\left(L_SS_ST+K\right)-\frac{L_S^2T\Delta T}{a_1}\cosh\frac{d_N}{\lambda}$. Equations (14) and (16) show clearly that the effect of the Joule heating on the power output and efficiency has been considered in the present model.

4. Maximum power output and efficiency

It can be proved by Eqs. (14) and (16) that $d_N/\lambda=0$, $V\lambda/L=0$, $d_N/\lambda\to\infty$, or $V\lambda/L\to\infty$, both P and η are equal to zero. This means that both P and η are not of monotonic functions of d_N/λ and $V\lambda/L$. Using Eqs. (14) and (16), we can plot the three-dimensional projection graphs of the power output density $P^*=P/A$ and efficiency η of the SSPD varying with $V\lambda/L$ and d_N/λ, as shown in Fig. 4.

Fig. 4(a) shows that there exist a maximum power output density $P_{\max}^*$ and the optimal values of $V\lambda/L$ and d_N/λ. The physical causes may be explained as follows. When the thickness d_N increases from zero, the spin current injecting into the normal metal increases quickly, leading to the increase of the average transverse charge current and the power output density. When d_N is large, the electromotive force generated by the inverse spin Hall effect will decrease as d_N increases continuously, resulting to the decrease of the average transverse charge current and the power output density. Thus, there is an optimal value for d_N/λ so that the

power output density attains its maximum. On the other hand, when $V\lambda/L$ is small, the increment of $V\lambda/L$ is larger than the reduction of the average transverse charge current, leading to the increase of the power output density. When $V\lambda/L$ is large, the increment of $V\lambda/L$ is less than the reduction of the average transverse charge current, resulting to the decrease of the power output density. Thus, the power output density firstly increases and then decreases as $V\lambda/L$ increases, and consequently, there is a maximum value of the power output density for the optimal value of $V\lambda/L$. Using Eq. (14), we can derive the optimal values of $V\lambda/L$ at the optimized power output density P_{opt} as

$$\left(\frac{V\lambda}{L}\right)_P = \frac{-c_2}{2c_1} = \frac{V_{open}\lambda}{2L}. \tag{17}$$

Equation (17) shows that $(V\lambda/L)_P$ is not a monotonic function of d_N/λ, as shown in Fig. 2 (b). In such a case, the optimized power output and the average transverse charge current at the optimized power output density are, respectively, given by

$$P_{opt} = \frac{c_2^2}{4c_1}, \tag{18}$$

and

$$\left(\frac{J_c L}{\lambda}\right)_P = \frac{-c_2}{2} = \frac{J_{c,sh}L}{2\lambda}. \tag{19}$$

Equation (19) indicates that like the average transverse charge current at the short circuit, the average transverse charge current at the optimized power output density is also a monotonically increasing function of d_N/λ, as shown in Fig.3(b). Using Eq. (18), one can conveniently generate the $d_N/\lambda \sim P_{opt}^*$ curve for different values of the spin Hall angle θ_{SH}, as shown in Fig.5.

Fig. 4(b) shows that there exist a maximum efficiency $\eta_{\max}$ and the optimal values of $V\lambda/L$ and d_N/λ. Using Eq. (16), we can derive the optimal values of $V\lambda/L$ at the optimized efficiency η_{opt} as

$$(V\lambda/L)_\eta = -(c_1c_4 + c_5)/(c_1c_3), \tag{20}$$

where $c_5 = \sqrt{-c_1c_2c_3c_4 + (c_1c_4)^2}$. In such a case, the value of J_cL/λ at the optimized efficiency and the optimized efficiency η_{opt} can be, respectively, derived as

$$\left(J_c L/\lambda\right)_\eta = (c_1c_4 + c_5)/c_3 - c_2 \tag{21}$$

and

$$\eta_{opt} = \frac{-c_2c_3(c_1c_4 + c_5) + (c_1c_4 + c_5)^2}{c_1c_4c_3^2 - c_3^2(c_1c_4 + c_5)}. \tag{22}$$

Using Eqs. (20)-(22), we can generate the curves of $\left(V\lambda/L\right)_\eta$, $\left(J_c L/\lambda\right)_\eta$, and η_{opt} varying with d_N/λ, as shown by Figs. 2(b), 3(b), and 5, respectively.

It can be seen from Fig. 5 that the optimized power output density P^*_{opt} and efficiency η_{opt} increase as θ_{SH} increases. With the increase of the doping of nonmagnetic metal, θ_{SH} can increase and the performance of the SSPD can be improved. Fig. 5 shows that for an SSPD, when the value of d_N/λ is designed to be equal to $(d_N/\lambda)_P$, the power output density can attain its maximum and the corresponding efficiency is equal to η_P; when the value of d_N/λ is designed to be equal to $(d_N/\lambda)_\eta$, the efficiency can attain its maximum and the corresponding power output density is equal to P^*_η; when $d_N/\lambda < (d_N/\lambda)_P$, both the power output density and the efficiency decrease with the decrease of d_N/λ; when $d_N/\lambda > (d_N/\lambda)_\eta$, both the power output density and the efficiency decrease with the increase of d_N/λ. It indicates that the regions of $d_N/\lambda < (d_N/\lambda)_P$ and $d_N/\lambda > (d_N/\lambda)_\eta$ are not optimal for an SSPD, because one always hopes to obtain a power output density and an efficiency as large as possible. Thus, the optimal region of an SSPD should be

$$\left(d_N/\lambda\right)_P \le d_N/\lambda \le \left(d_N/\lambda\right)_\eta. \tag{23}$$

It is clearly seen from Fig. 5 that both $(d_N/\lambda)_P$ and $(d_N/\lambda)_\eta$ are very close. Only when an SSPD is carefully designed, can d_N/λ be in the optimal region determined by Eq. (23). Combining Eq. (23) with Fig. 5, we can further determine the optimal regions of other parameters as

$$P^*_{\max} \ge P^* \ge P^*_\eta, \tag{24}$$

$$\eta_P \le \eta \le \eta_{\max}, \tag{25}$$

and

$$\left(V\lambda/L\right)_{\eta,m} \le V\lambda/L \le \left(V\lambda/L\right)_{P,m}, \tag{26}$$

where $(V\lambda/L)_{P,m}$ and $(V\lambda/L)_{\eta,m}$ are the values of $V\lambda/L$ at the maximum power output density and efficiency and can be calculated from Eq. (17) and $(d_N/\lambda)_P$ and Eq. (20) and $(d_N/\lambda)_\eta$, respectively. When an SSPD is operated in the region mentioned above, the power output density will decrease as the efficiency increases, and vice versa. These results show that $P^*_{\max}$, $\eta_{\max}$, η_P, P^*_η, $(d_N/\lambda)_P$, $(d_N/\lambda)_\eta$, $(V\lambda/L)_{P,m}$, and $(V\lambda/L)_{\eta,m}$ are some important parameters of the SSPD. It is seen from Eq. (26) that both V and λ/L are coupled together and their optimal regions are shown by the shaded area in Fig. 6.

According to the optimal criteria obtained above, one can availably choose the desired materials and optimally design the structure of an SSPD. Besides, one must control the voltage output of an SSPD which is directly dependent on the load resistance. Thus, it is necessary to discuss the optimal matching of the load resistance.

5. Load matching

From Fig. 1(b) and Eqs. (15) and (16), we can obtain the between the average transverse charge current J_c and the load resistance R_L as

$$J_c = V/R_L = E/(R_I + R_L). \tag{27}$$

By using Eqs. (11) and (27), V, E, and R_I can be, respectively, expressed as

$$V = \frac{-R_L c_2}{c_1 R_L \lambda/L + L/\lambda}, \tag{28}$$

$$E = -(c_2 L)/(c_1 \lambda) = V_{open}, \tag{29}$$

and

$$R_I = L^2/(\lambda^2 c_1). \tag{30}$$

From Eqs. (17), (20) and (28), we can derive the optimal values of $R_L W\lambda^2/L$ at the optimized power output density P_{opt} and the optimized efficiency η_{opt} as

$$(R_L W\lambda^2/L)_P = A/c_1 \tag{31}$$

and

$$\left(R_L W\lambda^2/L\right)_{\eta} = \frac{\left(c_1c_4 + c_5\right)A}{c_1\left[c_2c_3 - \left(c_1c_4 + c_5\right)\right]}. \tag{32}$$

Using Eqs. (26) and (30)-(32), we can determine the optimal regions of $R_L W\lambda^2/L$ and $R_I W\lambda^2/L$ as

$$\left(A/c_1\right)_{P,\mathrm{m}} = \left(R_L W\lambda^2/L\right)_{P,\mathrm{m}} \le R_L W\lambda^2/L \le \left(R_L W\lambda^2/L\right)_{\eta,\mathrm{m}} = \{(A/c_1)(c_1c_4 + c_5)/[c_2c_3 - (c_1c_4 + c_5)]\}_{\eta,m} \tag{33}$$

and

$$\left(A/c_1\right)_{P,\mathrm{m}} \le R_I W\lambda^2/L \le \left(A/c_1\right)_{\eta,\mathrm{m}}, \tag{34}$$

where $\left(R_L W\lambda^2/L\right)_{P,\mathrm{m}}$ and $\left(R_L W\lambda^2/L\right)_{\eta,\mathrm{m}}$ are the values of $R_L W\lambda^2/L$ at the maximum power output density and efficiency, and $(A/c_1)_{P,\mathrm{m}}$ and $(A/c_1)_{\eta,\mathrm{m}}$ are the values of $R_I W\lambda^2/L$ at the maximum power output density and efficiency. Eqs. (33) and (34) show that when the SSPD is operated at the maximum power output desnsity, the optimal matching condition of the load resistance is $R_L = R_I = \left(A/c_1\right)_{P,\mathrm{m}} L/(W\lambda^2)$, and that when the SSPD is operated at the maximum efficiency, the optimal matching condition of the load resistance is $R_L \approx R_I = \left(A/c_1\right)_{\eta,\mathrm{m}} L/(W\lambda^2)$ because $\{(c_1c_4 + c_5)/[c_2c_3 - (c_1c_4 + c_5)]\}_{\eta,m} = 0.9996 \approx 1$. Eq. (33) also shows that both R_L and $W\lambda^2/L$ are coupled together and their optimal regions are shown by the shaded area in Fig. 7. It means that the optimal value of the load resistance R_L is closely dependent on the choice of both W/L and λ. It is seen from Eq. (30) that the larger both W/L and λ are, the smaller the internal resistance R_I. λ is determined by the properties of materials and W/L is determined by the structure of the SSPD. Thus, one should choose the suitable materials, determine the rational structure of the SSPD, and match the load resistance so that $R_L W\lambda^2/L$ satisfy the criterion given by Eq. (33). When both W/L and λ are given, the optimal values of other parameters at the maximum power output density and efficiency can be determined and are listed in Table 1.

6. Conclusions

We have analyzed the performance characteristics of a nanoscale SSPD based on spintronics and spin caloritronics. It is found that the performance of the SSPD is dependent on not only the choice of materials and the structure of the normal metal but also the matching of the load resistance. Using the selective criteria of main parameters given above, we can optimally design an SSPD. Improving the spin Hall angle and the interface spin-exchange efficiency, we can further enhance the performance characteristics of the SSPD. The results obtained may provide a better understanding of the coupling between thermoelectric and thermomagnetic properties and help engineers design nanoscale spin Seebeck thermoelectric conversion devices and spin Peltier refrigerators in the future.

Acknowledgements

This work has been supported by the National Natural Science Foundation (No. 11175148), People's Republic of China.

References

[1] A. Majumdar. *Science*, 2004, 303, 777-778.

[2] K. Uchida, S.Takahashi, K. Harii, J. Ieda, W. Koshibae, K. Ando, S. Makawa, and E. Saitoh, 2008, 455, 778-781.

[3] E. Saitoh, M. Ueda, H. Miyajima, and G.Tatara. *Appl. Phys. Lett.*, 2006, 88, 182509.

[4] M. X. Zhai, X. F. Wang, P. Vasilopoulo, Y. S. Liu, Y. J. Dong, L. P. Zhou, Y. J. Jiang, and W. L. You. *Nanoscale*, 2014, 6, 11121.

[5] C. M. Jaworski, J. Yang, S. Mack, D. D. Awschalom, J. P. Heremans, and R. C. Myers. *Nat. Mater.*, 2010, 9, 898-903.

[6] A. Ozaeta, P. Virtanen, F. S. Bergeret, and T. T. Heikkilä. *Phys. Rev. Lett.*, 2014, 112, 057001.

[7] K. Uchida, J. Xiao, H. Adachi, J. Ohe, S. Takahashi, J. Ieda, T. Ota, Y. Kajiwara, H. Umezawa, H. Kawai, G. E. W. Bauer, S. Maekawa, and E. Saitoh. *Nat. Mater.*, 2010, 9, 894-897.

[8] A. Hoffman, *IEEE Trans. Magn.*, 2013, 49, 5172.

[9] Y. Tserkovnyak, A. Brataas, and G. E. Bauer. *Phys. Rev. Lett.*, 2002, 88, 117601.

[10] C. M. Jaworski, R. C. Myers, E. Johnston-Halperin, and J. P. Heremans. *Nature*, 2012, 487, 210-213.

[11] M. V. Costache, G. Bridoux, I. Neumann, and S. O.Valenzuela. *Nat. Mater.*, 2012, 11, 199.

[12] H. Adachi and S. Maekawa. *Solid State Commun.* 2014, 198, 22-25.

[13] S. Borlenghi, W. Wang, H. Fangohr, L. Bergqvist, and A. Delin. *Phys. Rev. Lett.*, 2014, 112, 047203.

[14] A. Kirihara, K. Uchida, Y. Kajiwara M. Ishida, Y. Nakamura, T. Manako, E. Saitoh, and S. Yorozu. *Nat. Mater.*, 2012, 11, 686-689.

[15] M. G. Zeng, W. Huang, and G. C. Liang. *Nanoscale*, 2013, 5, 200.

[16] F. Mahfouzi and B. K. Nikolić. *Phys. Rev. B*, 2014, 90, 045115.

[17] K. Nagai, Y. Cao, T. Tanaka, and K. Matsuyama. *J. Appl. Phys.*, 2012, 111, 07D130.

[18] J. Yang, K. M. Jiang, W. Y. Wu, and L. Chen. *Solid State Commun.*, 2013, 161, 46-49.

[19] S. M. Rezende, R. L. Rodríguez-Suárez, R. O. Cunha, A. R. Rodrigues, F. L. A. Machado, G. A. Fonseca Guerra, J. C. Lopez Ortiz, and A. Azevedo. *Phys. Rev. B*, 2013, 89, 014416.

[20] K. Uchida, H. Adachi, T. Ota, H. Nakayama, S. Maekawa, and E. Saitoh. *Appl. Phys. Lett.*, 2010, 97, 172505.

[21] K. Uchida, T. Nonaka, T. Kikkawa, Y. Kajiwara, and E. Saitoh. *Phys. Rev. B*, 2013, 87, 104412.

[22] M. Agrawal, V. I. Vasyuchka, A. A. Serga, A. Kirihara, P. Pirro, T. Langner, M. B. Jungfleisch, A. V. Chumak, E. Th. Papaioannou, and B. Hillebrands. *Phys. Rev. B.*, 2014, 89, 224414.

[23] T. Kikkawa, K. Uchida, Y. Shiomi, Z. Qiu, D. Hou, D. Tian, H. Nakayama, X. F. Jin, and E. Saitoh. *Phys. Rev. Lett.*, 2013, 110, 067207.

[24] Y. D. Xu, B. W. Yang, C. Tang, Z. L. Jiang, M. Schneider, R. Whig, and Jing Shi. *Appl. Phys. Lett.*, 2014, 105, 242404.

[25] J. B. S. Mendes, R. O. Cunha, O. Alves Santos, P. R. T. Ribeiro, and F. L. A. Machado. *Phys. Rev. B*, 2014, 89, 140406(R).

[26] S. M. Rezende, R. L. Rodríguez-Suárez, and A. Azevedo. *Phys. Rev. B*, 2014, 89, 094423.

[27] S. M. Rezende, R. L. Rodríguez-Suárez, J. C. Lopez Ortiz, and A. Azevedo. *Phys. Rev. B*, 2014, 89, 134406.

[28] P. Li, D. Ellsworth, H. C Chang, P. Janantha, D. Richardson, F. Shah, P. Phillips, T. Vijayasarathy, and M. Z Wu. *Appl. Phys. Lett*., 2014,105, 242412.

[29] J. Flipse, F. K. Dejene, D. Wagenaar, J. B. Youssef, and B. J. van Wees. *Phys. Rev. Lett*., 2014, 113, 027601.

[30] A. B. Cahaya, O. A. Tretiakov, and G. E. W. Bauer. *Appl. Phys. Lett.*, 2014, 104, 042402.

[31] D. J. Standers and D. Walton. *Phys. Rev. B*, 1977, 15, 1489.

[32] S. M. Rezende, R. L. Rodríguez-Suárez, R. O. Cunha, A. R. Rodrigues,1 F. L. A. Machado, G. A. Fonseca Guerra, J. C. Lopez Ortiz, and A. Azevedo. *Phys. Rev. B*, 2014, 89, 014416.

[33] M. Agrawal, V. I. Vasyuchka, A. A. Serga, A. D. Karenowska, G. A. Melkov, and B. Hillebrands. *Phys. Rev. Lett*., 2013, 111, 107204.

[34] B. Liao, J. W. Zhou, and G. Chen. *Phys. Rev. Lett*., 2014, 113, 025902.

[35] M. Schreier, A. Kamra, M. Weiler, J. Xiao, G. E. W. Bauer, R. Gross, and S. T. B. Goennenwein. *Phys. Rev. B.*, 2013, 88, 094410.

[36] A. Brataas, Y. V. Nazarov, and G. E.W. Bauer. *Phys. Rev. Lett.*, 2000, 84, 2481.

[37] M. Johnson and R. H. Silsbee. *Phys. Rev. B*, 1988, 37, 5312.

Figure captions

Fig. 1. (a) The schematic diagram and (b) the effective circuit of an SSPD.

Fig. 2. (a) The three dimensional projection graph of V_{open} varying with d_N/λ and L/λ and (b) the curves of $V\lambda/L$ at the open circuit, maximum power output, and maximum efficiency varying with d_N/λ, where $G_N/A=10^{15}\,\Omega^{-1}\mathrm{m}^{-2}$, $G_S/A=6\times10^{13}\,\Omega^{-1}\mathrm{m}^{-2}$, $L_S/A=4\times10^{9}\,\mathrm{AK}^{-1}\mathrm{m}^{-2}$, $\theta_{SH}=0.1$, $T_{\mathrm{b}}^{\mathrm{p}}=300\,\mathrm{K}$, and $T_{\mathrm{t}}^{\mathrm{e}}=295\,\mathrm{K}$ are chosen [30].

Fig. 3. (a) The three dimensional projection graph of $J_{c,sh}$ varying with d_N/λ and L/λ and (b) the curves of J_cL/λ at the short circuit, maximum power output, and maximum efficiency varying with d_N/λ, where the values of other parameters are the same as those used in Fig.2.

Fig. 4 Three-dimensional graphs of (a) the power output density P^* and (b) efficiency η of the SSPD as the functions of $V\lambda/L$ and d_N/λ, where the values of other parameters are the same as those used in Fig. 2.

Fig. 5. The curves of the optimized power output density P_{opt}^* and the optimized efficiency η_{opt} versus d_N/λ for different values of the spin Hall angle θ_{SH}, where the values of other parameters are the same as those used in Fig. 2.

Fig. 6. The $\lambda/L\sim V$ curves satisfying $V\lambda/L=(V\lambda/L)_{P,m}$ and $(V\lambda/L)_{\eta,m}$, where the optimal values of V and λ/L are determined by the shaded region surrounded by two curves.

Fig. 7. (a) The $W\lambda^2/L\sim R_L$ curves satisfying $R_LW\lambda^2/L=(R_LW\lambda^2/L)_{P,\mathrm{m}}$ and $(R_LW\lambda^2/L)_{\eta,\mathrm{m}}$, where the optimal values of R_L and $W\lambda^2/L$ are determined by the shaded region surrounded by two curves.

Table caption

Table 1. The optimal values of some parameters at the maximum power output density and efficiency.

Fig. 1.

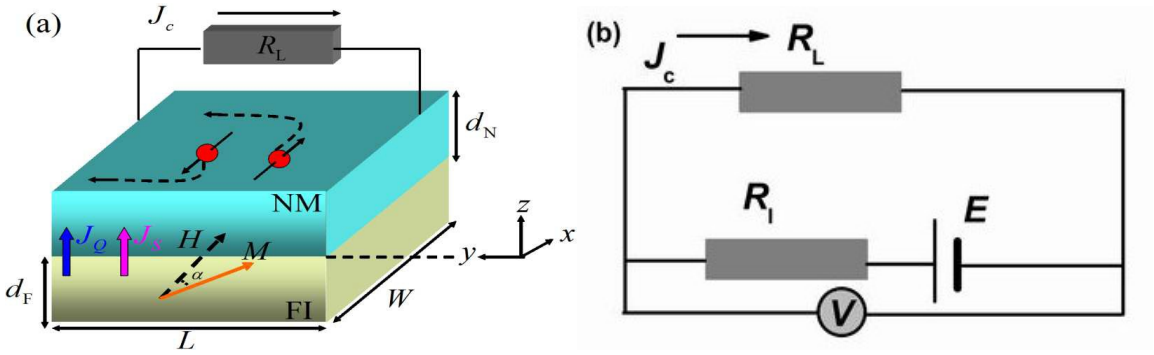

Fig. 2.

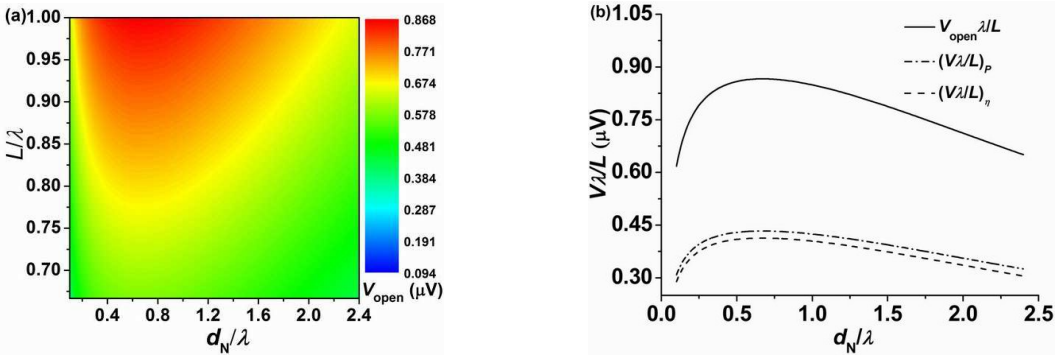

Fig. 3.

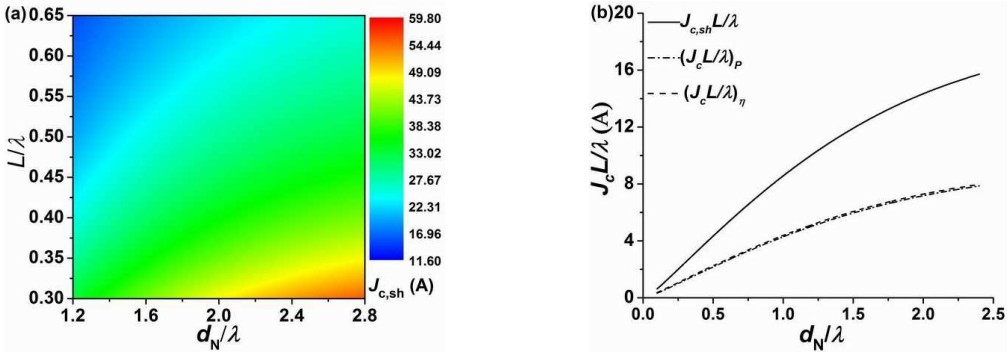

Fig. 4

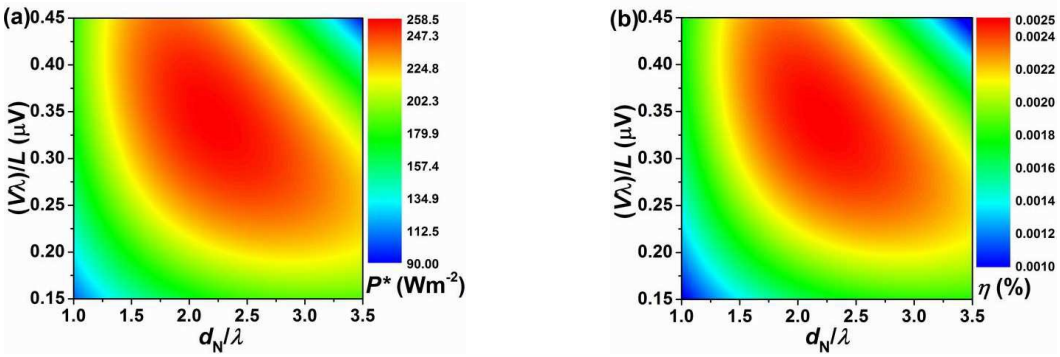

Fig. 5

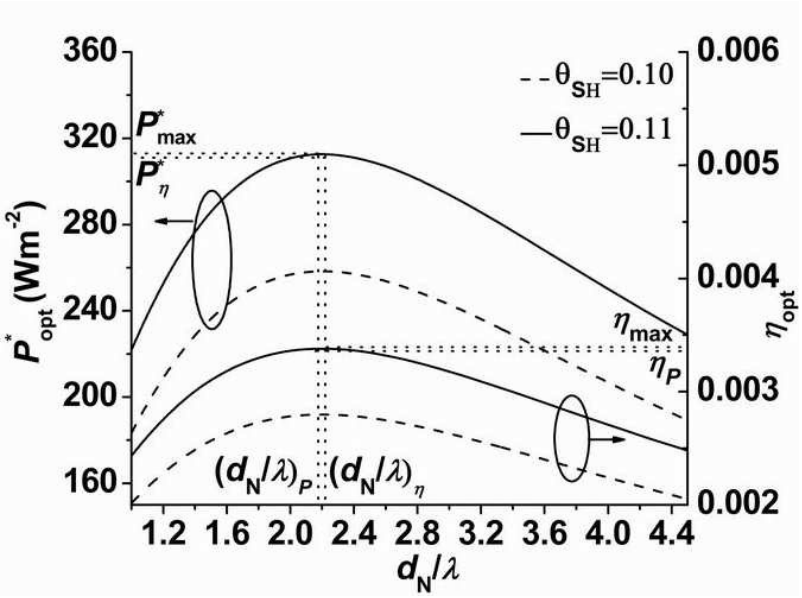

Fig. 6.

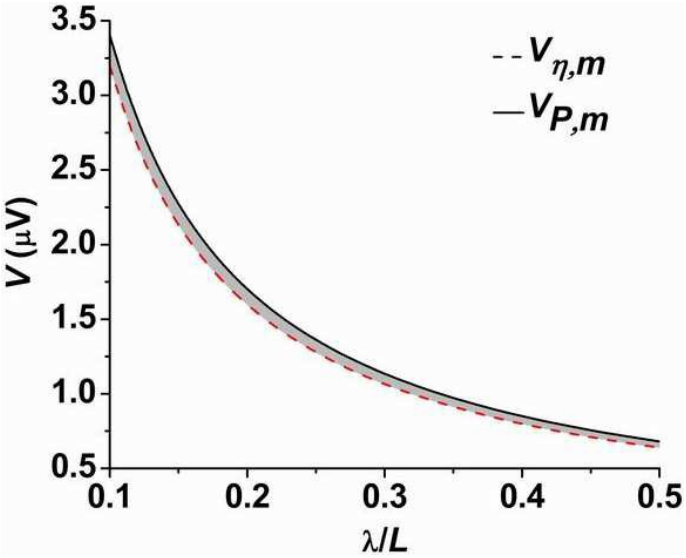

Fig. 7.

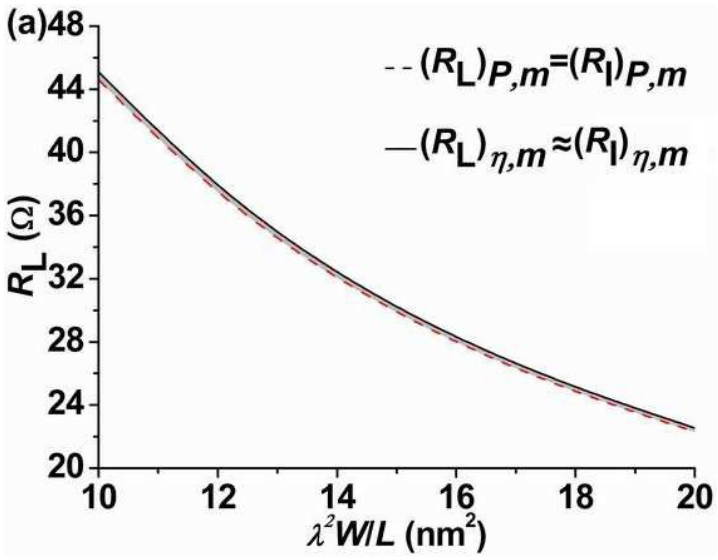

Table 1.

$P^*_{\max}$	$\eta_{\max}$ (%)	λ (nm)	$(d_N)_{P,m}$ (nm)	$(d_N)_{\eta,m}$ (nm)	W/L	$(R_L)_{P,m} = (R_I)_{P,m}$	$(R_L)_{\eta,m} \approx (R_I)_{\eta,m}$
259	0.0025	1.4	3.07	3.11	5	45.9	46.3
					10	22.9	23.1
					15	15.3	15.4
		1.5	3.29	3.33	5	39.9	40.3
					10	20.0	20.2
					15	13.3	13.4
		1.6	3.50	3.55	5	35.1	35.4
					10	17.6	17.7
					15	11.7	11.8